Results in Engineering 13 (2022) 100313

Contents lists available at ScienceDirect

Results in Engineering

journal homepage: www.sciencedirect.com/journal/results-in-engineering

Visible Light Photocatalytic Activity of Ag/WO_3 Nanoparticles and its Antibacterial Activity Under Ambient Light and in The Dark

Maha Matalkeh [a], Gheyath K. Nasrallah [b,c], Farah M. Shurrab [b], Enas S. Al-Absi [b], Widad Mohammed [d], Ahmed Elzatahry [d], Khaled M. Saoud [a,*]

[a] Liberal Arts and Science, Virginia Commonwealth University School of Arts in Qatar, P.O. Box 8095, Doha, Qatar
[b] Biomedical Research Center, Qatar University, Doha, 2713, Qatar
[c] Department of Biomedical Science, College of Health Sciences, Member of QU Health, Qatar University, P.O. Box 2713, Doha, Qatar
[d] Material Science and Technology Program, College of Arts and Sciences, Qatar University, 2713, Doha, Qatar

A B S T R A C T

Nanomaterial such as metals and metal oxide photocatalysts have emerged as important tools for removing contaminants from wastewater and as antibacterial agents to prevent infections; this is mainly due to their stability under different irradiation conditions. Herein, the catalytic and antimicrobial activities of nanocrystalline silver (Ag), supported on tungsten oxide (WO_3) nanoparticles prepared using the deposition-precipitation synthesis technique, are studied. The synthesized material was characterized as XRD, XPS, TEM, and TEM-EDS to investigate their physio-chemical properties. HRTEM, XPS analysis shows that the photocatalyst has a large sheet-like morphology with well-dispersed small metallic Ag particles (<3 nm) on the WO_3 nanoparticle's surface, with most particles near the edges. Ultraviolet–visible spectra analysis observed a large redshift in the absorbing band edge and decreased bandgap energy from 2.6 to 2.1 eV. Photocatalytic analysis at different concentrations of 1% Ag/WO_3 under visible light indicated a high degradation efficiency. The largest degradation efficiency of Methylene Blue (MB) under visible light irradiation was (~80%) in 120 min at 1 g/L catalyst dosage. The photodegradation of MB under visible light as a function of catalyst dose followed the pseudo-first-order kinetics. In addition, the catalyst shows high degradation efficiency and significant dose-dependent inhibition of Gram-negative E. Coli and the Gram-positive *S. aureus*. Furthermore, the catalyst showed excellent stability and recyclability.

1. Introduction

Recent studies suggest that contaminants such as pharmaceuticals, phenolic compounds, and dyes are found in water sources, while microorganisms grow in water and on surfaces. Phenolic derivatives, polycyclic aromatic compounds, extractants, analytical reagents, and dyes are all organic pollutants found in the environment [1]. Dyes such as MB are among the most harmful pollutants released from textile, paint, paper, and plastic industries [2]. Photocatalysts have received considerable attention in recent years due to their environmental and biomedical application. Using a photocatalyst such as TiO_2 shows great promise for destroying contaminants and microorganisms under various irradiation conditions. Heterogeneous metal and metal oxide semiconductor photocatalysts have been widely used in water and air pollutants abatement. Furthermore, they show excellent efficiency in removing organic pollutant dyes, pesticides, and pharmaceuticals under ultraviolet (UV) light irradiation [3,4]. The popular antibacterial activity of metals (Ag, Au, and Cu) along with the visible light-activated reactive oxygen species production in semiconductor metal oxide (ZnO, WO_3, and TiO_2) nanocomposites promises enhanced antibacterial and antiviral activities [5–7]. Photocatalytic activity is highly dependent on the ability of the catalyst to create electron-hole pairs. This process generates free radicals (hydroxyl radicals: ·OH) that can undergo secondary reactions. Organic compounds such as bacteria and viruses or toxic materials can be effectively degraded and combusted into CO_2 and H_2O through photocatalysis using semiconducting nanoparticles. Metal oxide nanoparticles such as TiO_2, zinc oxide (ZnO), and tungsten oxide (WO_3) have been extensively used for degrading bacteria and viruses or toxic contaminants by exposing them to UV light illumination [8]. TiO_2 is a well-known photocatalytic material and has been used commercially. Even though TiO_2 is cost-effective, stable, and corrosion resistant, its high bandgap energy of 3.2 eV, which requires high UV irradiation for excitation, limits its application in the visible-light region of the solar spectra. As an alternative, WO_3 is a nontoxic, chemically, and photochemically stable semiconductor in aqueous media over many pH values. WO_3 is an n-type tungsten oxide semiconductor with a narrow bandgap in the range of (2.6–2.8 eV) eV [9,10], and it can be activated by visible light irradiation [11]. Tungsten

* Corresponding author.
E-mail address: s2kmsaou@vcu.edu (K.M. Saoud).

https://doi.org/10.1016/j.rineng.2021.100313
Received 5 October 2021; Received in revised form 2 December 2021; Accepted 3 December 2021
Available online 22 December 2021

oxide can form different compounds (i.e., WO_3, WO_2, and none-stoichiometric oxide) due to the presence of multiple oxidation numbers [12]. As a result, WO_3 can possess several excellent photocatalytic, chemical, electrical, and antibacterial properties [13–16]. However, due to the high recombination rate of the photogenerated (e^-/h^+) pairs, WO_3 has limited long-term photocatalytic activity. Recently, researchers have been focusing on visible light photocatalysis that constitutes a significant share (~46%) of the solar spectrum compared to UV light (~7%) [17]. Photocatalysis using visible light has been reported to be possible by doping semiconductors with transition metals to reduce the effective bandgap [18]. Several metallic elements have been used as a dopant to modify the electronic structure and surface properties of WO_3, extending their visible light region absorbance and the photocatalyst's lifetime. This process is achieved by trapping photogenerated electrons to create valence band (VB) holes that oxidize the organic molecules rather than consuming them in a recombination reaction [19,20]. Ag supported on metal oxides such as ZnO showed significant photocatalytic activities under different irradiation conditions and dark [21,22]. The damaged cell membrane and DNA degradation were observed only under illumination due to the photocatalytic electron injection process, while inactivation in the dark is primarily attributable to Ag and ZnO's bactericidal effect ions [22]. Ag plays a vital role in enhancing the photocatalytic activity of WO_3 activity due to improved charge separation and electron-hole recombination reduction. Ag nanoparticles' localized surface plasmon resonance absorption leads to visible light photocatalytic activity [23–26,28].

The efficient visible light photodecomposition of methylene blue (MB) as a probe contaminant was investigated. Herein, the synthesis and characterization of Ag/WO3 with 1% Ag loading is reported. Moreover, the inactivation of *Staphylococcus aureus* and *Escherichia coli* on Ag/WO_3 under ambient light and in the dark is reported. This study presents highly efficient photocatalysts for the degradation of organic pollutants and microorganisms. The synthesized material acts as an antimicrobial to inhibit bacteria and viruses under ambient light and dark conditions to remove microorganisms from water resources and surfaces and protect people against growing infectious diseases. This process is green and based on bio-mimicking photosynthesis by employing visible light (sunlight or ambient light), photocatalysis, and nanotechnology.

2. Experimental

2.1. Materials

Tungsten oxide (WO_3, Hongwu Nano), Silver nitrate ($AgNO_3$; HIMEDIA), Sodium borohydride ($NaBH_4$, Fisher Scientific), Cetrimonium bromide (CTAB; Sigma Aldrich), L-ascorbic acid (L-ASA; NICE Chemicals (P) LTD.), Ethanol (EtOH; Fisher Chemicals), ultra-pure water (UPW; 18.1 MΩ-cm; Thermo Scientific) were all used without any further purification.

2.2. Catalyst synthesis

To decorate Ag nanoparticles on a WO_3 surface, the deposition-precipitation method was used (Scheme 1). Typically, 3 g of WO_3 was first ultrasonically dispersed in a 100 ml mixture solution containing ultrapure (UP) water and absolute ethanol with a volume ratio of 1:1 for 15 min in a 250 ml beaker. 0.01 g CTAB and a certain amount of $AgNO_3$ were dissolved in 20 ml UP water, and absolute ethanol with a volume ratio of 1:1 was added to the resultant solution under vigorous stirring; the stirring was continued for another 30 min. After that, 25 ml of 0.05 M L-ascorbic acid was added into the above solution and left stirring for 1.5 h. Consequently, Ag nanoparticles are deposited on the WO_3 surface. The product was collected by vacuum filtration and then dried for 24 h at 60 °C after washing several times with UP water and absolute ethanol. Ag/WO_3 was obtained by calcining at 300 °C in the air for 1 h using a muffle furnace to remove undesirable substances. For comparison, Ag/WO_3 was synthesized without calcination treatment.

2.3. Catalyst characterization

Several techniques were used to characterize WO_3 and Ag (0.1%, 0.5%, 1%) loaded WO_3 photocatalysts. The elemental analysis and actual Ag loading were measured using inductively coupled plasma optical emission spectroscopy (ICP-OES) (iCAP 6000 series, Thermo Scientific, USA) synthesized photocatalyst samples. The N_2-sorption analysis was performed using Micromeritics ASAP2020 Accelerated Surface Area and Porosimetry System (Micro metrics, Norcross, GA, USA) at 77 K, and specific surface area and the pore size distribution were determined using the Brunauer–Emmett–Teller (BET) and Barrett–Joyner–Halenda (BJH) methods, respectively. The structure, crystallography, and phase of synthesized catalyst analysis of the photocatalyst were carried out using X-ray diffraction (XRD) (X'Pert PRO X-ray diffractometer, USA) with Cu-Kα X-ray ($\lambda = 0.15418$ nm), ranging from 10° to 80°. High-resolution transmission electron microscopy (HRTEM) was performed using (FEI Talos 200X) operated at 200 kV, and energy-dispersive (EDS) (Thermofisher Scientific, USA) was employed to study morphology and elemental analysis of the prepared catalysts. X-ray photoelectron spectroscopy (XPS; Omicron Nanotechnology, Germany) was used to measure the silver nanoparticles' concentration and surface state, and Casa XPS software was used in data analysis and peak fitting. The obtained XPS spectra were calibrated to the C1s feature at 284.6 eV. The UV–visible absorption spectra of prepared samples were obtained by a split-beam UV–visible spectrophotometer (YK Scientific, UV1810/UV1810S, China). The Fourier-transform infrared spectroscopy (FTIR) measurements were recorded using an FTIR spectrometer (FTIR-650, Australia).

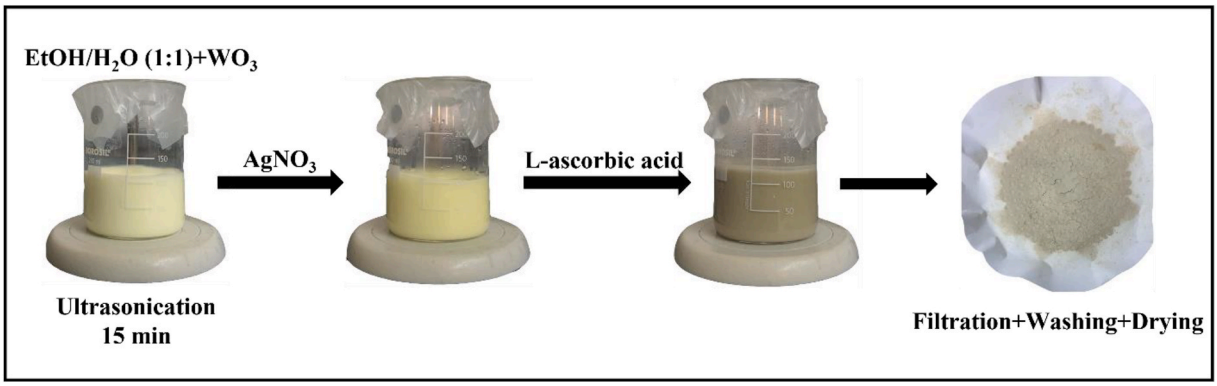

Scheme 1. The schematic diagram for the preparation of 1% Ag/WO_3 catalyst.

2.4. Photocatalytic activity test

All Ag/WO_3, synthesized samples, and WO_3 were tested for their photocatalytic activity toward MB dye degradation in the presence of sodium borohydride ($NaBH_4$) [27]. The rationale behind using $NaBH_4$ as a reducing agent is to accelerate the photocatalytic degradation process and bleach the solution photodegradation experiment, visible light irradiation using a 400 W ($\lambda \geq 400$) halogen lamp with an irradiation intensity of 1413.4 W/m^2. The lamp and the beaker were 15 cm apart. In a typical procedure, different amounts of the photocatalyst (0.02, 0.04, 0.1, and 0.2 g) were suspended in 200 ml MB (5.0 mg/L) solution in a 250 ml beaker in the presence of 1 ml 0.1 M $NaBH_4$. The solution was stirred in the dark for 30 min until irradiation to achieve equilibrium of absorption and desorption processes between the prepared photocatalyst and the MB. MB dye degradation was determined by recording and analyzing the UV–visible spectra at 664 nm, MB dye absorbance maximum wavelength, for 60 min every 10 min intervals. In the control experiment, the aqueous solution was irradiated in the absence of any photocatalyst. The blank used in all experiments was composed of UP water and $NaBH_4$. A UV–visible spectrometer was used to monitor the liquid after centrifuging 4 ml of suspension to separate the catalyst during the experiment.

A reaction can be zero, first, or second-order, depending on the contaminant concentration on the reaction rate. This process is found to be first order, based on kinetic models of photocatalytic processes. The Langmuir-Hinshelwood model is a kinetic model used to represent first-order reactions.

The degradation data were fit according to the pseudo-first-order kinetics:

$$\ln(C/C_0) = Kt \quad (1)$$

C is the concentration of MB at time t, C_0 is the original concentration of MB, and K is the reaction rate constant [22].

The line slope is equal to the rate constant of the first-order reaction if the graph of (Ln (C/C_0)) against time is displayed as a straight line.

The efficiency of MB dye degradation has been determined as follows:

$$\boldsymbol{R} = \left(1 - \frac{\boldsymbol{C}}{\boldsymbol{C_0}}\right) \times 100\% \quad (2)$$

R is photocatalytic efficiency, and Co and C (g/L) is the reactant concentration of aqueous MB solution initially and after time t, respectively [22].

2.5. Antibacterial activity test

An overnight culture of *Escherichia coli* (*E. coli*) and *Staphylococcus aureus* (*S. aureus*) were prepared by inoculating one colony in 3 ml Luria-Bertani (LB) broth medium and incubated in the shaker at 37 °*C* at 200 rpm. A 15 ml 1 g/L 1% Ag/WO_3 stock was prepared and sonicated for 10 min. A total of four working concentrations (0, 0.1, 0.2, 0.5, and 1 g/L) were then prepared in a total volume of 3 ml to test the antibacterial effect.

The antibacterial effect of 1% Ag/WO_3 was tested in ambient light (60 W) and dark conditions. For dark conditions, the tube was wrapped with aluminum foil. 1% of the primary bacterial culture (*E. coli* and *S. aureus*) was added to a secondary culture tube with different 1% Ag/WO_3 concentrations (0–1 g/L). Then, all tubes were incubated in the shaker at 37 °*C*, and the absorbance was measured each hour until the bacterial growth reached the early stationary phase (about 6hr). The absorbance was measured in triplicates for each concentration at zero time at an optical density of 600 nm. The OD readings were graphed as the average of three readings against time (hr) for each concentration. Two-way ANOVA, Dunnett's multiple comparisons test, was conducted to test for statistical significance. A p-value less than $\leq$0.05 is statistically significant. All the analysis was performed using GraphPad Prism Version 9.0.2.

3. Results and discussion

3.1. Catalyst characterization

The nitrogen adsorption/desorption isotherms of the samples have been recorded and shown in Fig. S1. The data of the specific surface areas of these samples with the corresponding pore sizes and pore volumes are summarized in Table 1. The WO_3 had a surface area of 19.8 m^2 g^{-1} and a pore size of 13.7 nm, while the 1% Ag/WO_3 sample had a surface area and a pore size of 19.4 m^2 g^{-1} and 17.7, respectively. The BET specific surface area of 1% Ag/WO_3 was slightly decreased. The decrease in the surface area could be attributed to the deposition of Ag nanoparticles, where it blocked the pore channels of WO_3, resulting in the pore channels being blocked [29].

The crystalline microstructure of synthesized Ag/WO_3 samples was analyzed using X-ray diffraction (XRD) (XPERT PRO), using the Cu Ka wavelength of 1.5405 Å, as shown in Fig. 1. The observed XRD pattern of the Ag/WO_3 photocatalyst reveals that the sample has the three most substantial well-defined diffraction peaks centered at 2θ = 23.25, 23.913, and 24.3), confirming the presence of monoclinic crystal structure with d-spacing 0.38, 0.364, and 0.360 nm, the (002), (020), and (200) refractions, respectively. However, the diffraction peaks corresponding to metallic silver Ag^0 or silver oxides Ag^{1+} are not observed, suggesting the presence of a very small silver particle size (2–5 nm) [32]. The XRD analysis revealed that all peaks matched perfectly with the diffraction lines for the monoclinic tungsten oxide (JCPDS 43–1035) [31], and no silver peaks according to (JCPDS 04–0783) were found in the XRD pattern other than impurity peaks. Moreover, a slight peak shift was observed for lower 2θ which could indicate the presence of small (<3 nm) and well-dispersed Ag nanoparticles that could not be detected due to the XRD detection limit (<3 nm).

The morphology, shape, size, distribution of the Ag and WO_3 particles, and the formation of Ag/WO_3 nanoparticles were investigated by the TEM-EDS spectra' compositions (Fig. 2) and used to determine the chemicals present in the synthesized samples. Elemental analysis confirms the presence of silver in the Ag/WO_3 composite. The EDS spectra consist of different Ag, C, Cu, S, O, and W peaks. The Cu peak came from the Cu TEM grids, and the C peak came from the carbon-coated copper grid, as shown in Fig. 2 (a). The silver and oxygen distribution on WO_3 was evaluated by quantitative EDS mapping and illustrated by HRTEM figure and scanning TEM (STEM)–high-angle annular dark-field (HAADF), images and EDS analysis, and mapping of elemental mapping of the Ag/WO_3 photocatalyst catalyst using pseudo-color representations to distinguish different elements, respectively. Fig. 2(c–g) represents the elemental mapping of C, W, O, and Ag in the sample where the main elements with a small percentage of Cu. These results confirm the presence of Ag at the surface and within the WO_3. It is important to note that the atomic percentage of Ag on the surface is higher than the Ag percentage in the entire sample.

HRTEM results are depicted in Fig. 3. It is clearly shown that the irregular shape and size of particles with the majority of WO_3 particles exhibit sheet-like morphology with a size larger than 500 nm and very few spherical particles about 150–200 nm. HRTEM revealed that the Ag nanoparticles are composed of highly dispersed and tiny silver nanoparticles (<3 nm), and large Ag particles with the size of 3–10 are

Table 1
BET surface areas and pore sizes of bare WO_3 and photocatalyst.

Material	BET specific surface area (m^2 g^{-1})	pore size (nm)
WO_3	19.8	13.7
1% Ag/WO_3	19.4	17.7

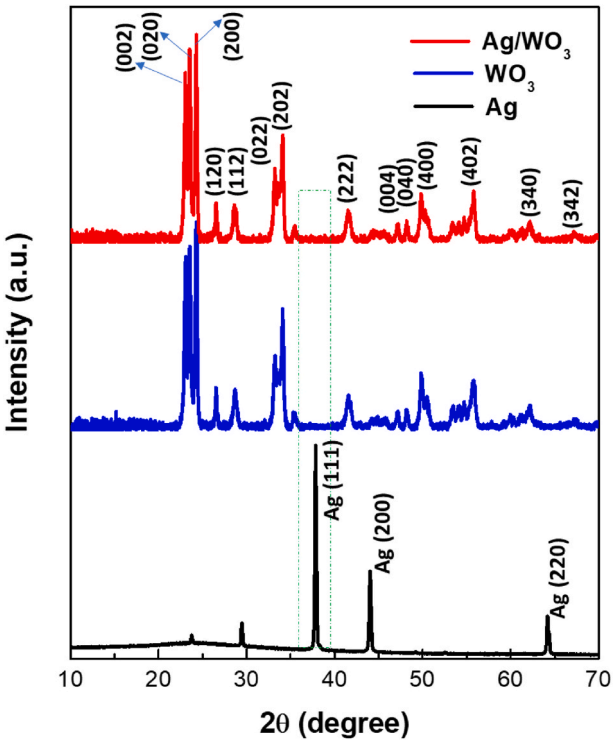

Fig. 1. XRD pattern of WO_3 tungsten oxide containing 1% Ag loadings compared to pure silver and tungsten oxide.

anchored and dispersed on the WO_3 surface nanosheets [30], as shown in Fig. 3(a and b). Selected area electron diffraction (SAED) (Fig. 3(c)) was performed to confirm the existence of Ag in WO_3 further, which clearly showed the existence of a combination of the spots, as observed in Fig. 3 (c), where the more substantial spot is attributed to underlying crystalline WO_3, confirming the presence of well-crystallized Ag particles [31]. These results complement the XRD results. The analysis of HRTEM images Fig. 3(d–f) confirms that the lattice fringe spacing of Ag-doped WO_3 is 3.8 nm for crystal plane [020] [23] and 3.64 nm for the crystal plane [002], corresponding to the lattice planes of WO_3 with the monoclinic structure [32].

XPS was used to study and analyze the chemical states and compositions of the Ag/WO_3 nanoparticles' surface, where the photocatalytic reaction mostly occurs. The XPS profiles of Ag/WO_3 are shown in Fig. 4, which indicates the chemical components and the corresponding binding energy levels. Fig. 4 (a) depicts the full scan profile of the materials' total composition, which showed W, Ag, and O, while C and a small amount of Na were probably due to contamination in the sample. The high-resolution XPS spectra of W 4f, Ag 3d and O 1s were deconvoluted and shown in Fig. 4 (b)–(d), respectively. Two spin-orbit doublets for W valence state W $4f_{7/2}$ and W $4f_{5/2}$ are observed at 35.8 eV and 37.9 eV, respectively, with 2.1 eV doublet splitting. Deconvolution of W $4f_{5/2}$ and W $4f_{7/2}$ spectra showed mostly W^{6+} peak present at 35.8 eV and 37.9 eV, respectively, suggesting tungsten stoichiometric tungsten. XPS peak analyses of Ag 3d in the fresh sample clearly show the silver consists mainly of metallic silver with two spin-orbit doublets corresponding Ag $3d_{5/2}$ and Ag $3d_{3/2}$ at binding energy values of 368.3 eV and 374.3 eV, respectively, with 6.0 eV doublet splitting [33]. The large splitting of the Ag 3d doublet of 6.0 eV suggests that the Ag exists in the form of metallic Ag. Deconvolution of Ag $3d_{5/2}$ and Ag $3d_{3/2}$ spectra showed Ag0 (metallic Ag) presence at binding energies of 368.3 eV and 374.3 eV, respectively. Similar results were reported previously [34]. The O 1s spectrum exhibited a peak at a binding energy of 530.6 and fit well with the oxygen bound to W^{6+} in the stoichiometric WO_3 phase [35]. These results confirm a small fraction of metallic silver dispersed in the NPS, as was shown in SEM, EDS, and TEM analysis.

3.2. UV–visible analysis

To examine the optical behavior of bare and Ag-loaded WO_3 nanoparticles, UV–visible spectroscopy measurements were carried out. Fig. 5 (a) displays the optical absorption spectra of prepared samples obtained with a UV–Vis spectrophotometer in the 300–1100 nm wavelength range. After the infusion of Ag nanoparticles into WO_3 nanoparticles, the absorption band edge of bare WO_3 is redshifted (towards a longer wavelength) [36]. Therefore, the material's bandgap energy was reduced due to the shifting of absorption band edges caused by Ag loading. The bandgap energy (E_g) values have been determined using the optical absorption data using the Tauc relation:

$$(\alpha h\nu) = A_0(h\nu - E_g)^n \quad (3)$$

A_o is a constant that corresponds to the fundamental band-band transitions, ν is the frequency of the incident photon, E_g is the bandgap energy value, and n is an index depending on the optical transition (direct or indirect) [37]. The direct bandgap of WO_3 and Ag-loaded WO_3 (Fig. 5(b)) was anticipated from the extrapolation of the linear part of hν vs. $(\alpha h\nu)^2$ for the absorption coefficient α [38]. The bandgap energy of WO_3 was 2.57 eV, which matched the literature [39]. The bandgap energy of Ag (0.1%, 0.5%, 1%) loaded WO_3 was calculated to be 2.41, 2.19, and 2.08, respectively. The bandgap energy of WO_3 nanoparticles decreases as Ag loading increases. A similar trend has also been reported in the literature [25,40,41], where different Ag loadings on WO_3 were studied. As a result, 1% Ag/WO_3 nanoparticles absorb more energy and excite more electrons from the valence band to the conduction band (CB) than bare WO_3 nanoparticles [36].

4. Photocatalytic degradation of analysis of MB

The catalytic reduction of MB dye by Ag/WO_3 catalysts in the presence of $NaBH_4$ can be explained using the electron transfer effect. Ag is a good conductor, allowing electrons to be transferred between donors and receptors. As a result, Ag nanoparticles can trigger this catalytic process through redox reactions, and electrons can be transferred from the BH_4^- as the donor to MB as the acceptor [42]. The effect of the $NaBH_4$ MB dye reduction process was investigated. The degradation curves with and without $NaBH_4$ at 1 g/L Ag/WO_3 dose under visible light irradiation and similar conditions are compared, as shown in Fig. S2. The results suggest a faster degradation in the presence of $NaBH_4$. All the experiments in this work were performed in the presence of $NaBH_4$.

4.1. Effect of metal loading

The capacity of bare and Ag (0.1%, 0.5%, 1%) loaded WO_3 photocatalysts to degrade aqueous MB solution under visible light irradiation was tested. Fig. 6 (a) shows the relative (C_t/C_0) concentration of MB versus the reaction time, which represents the response of photocatalytic activities of bare and Ag (0.1%, 0.5%, and 1%) loaded WO_3 catalysts. Ag-loaded WO_3 catalysts with various loading concentrations had higher photocatalytic activity than bare WO_3 catalysts, with 1% Ag/WO_3 being the highest activity among them after 60 min. In Fig. 6 (b), the degradation data were fit using pseudo-first-order kinetics. Table 2 summarizes the reaction rate constant, degradation efficiencies for bare WO_3, Ag (0.1%, 0.5%, 1%) loaded WO_3 photocatalysts and MB without catalyst. The photocatalytic degradation reaction rate constants using 0.1% Ag/WO_3 (0.01366 min^{-1}), 0.5% Ag/WO_3 (0.0141 min^{-1}), and 1% Ag/WO_3 (0.01637 min^{-1}) are all higher than WO_3 (0.01278 min^{-1}) and MB without photocatalyst (0.00269 min^{-1}). The photocatalytic activity of 1% Ag/WO_3 is the best, being 1 time faster than bare WO_3. The degradation efficiencies achieved using Ag (0.1%, 0.5%, and 1%) loaded

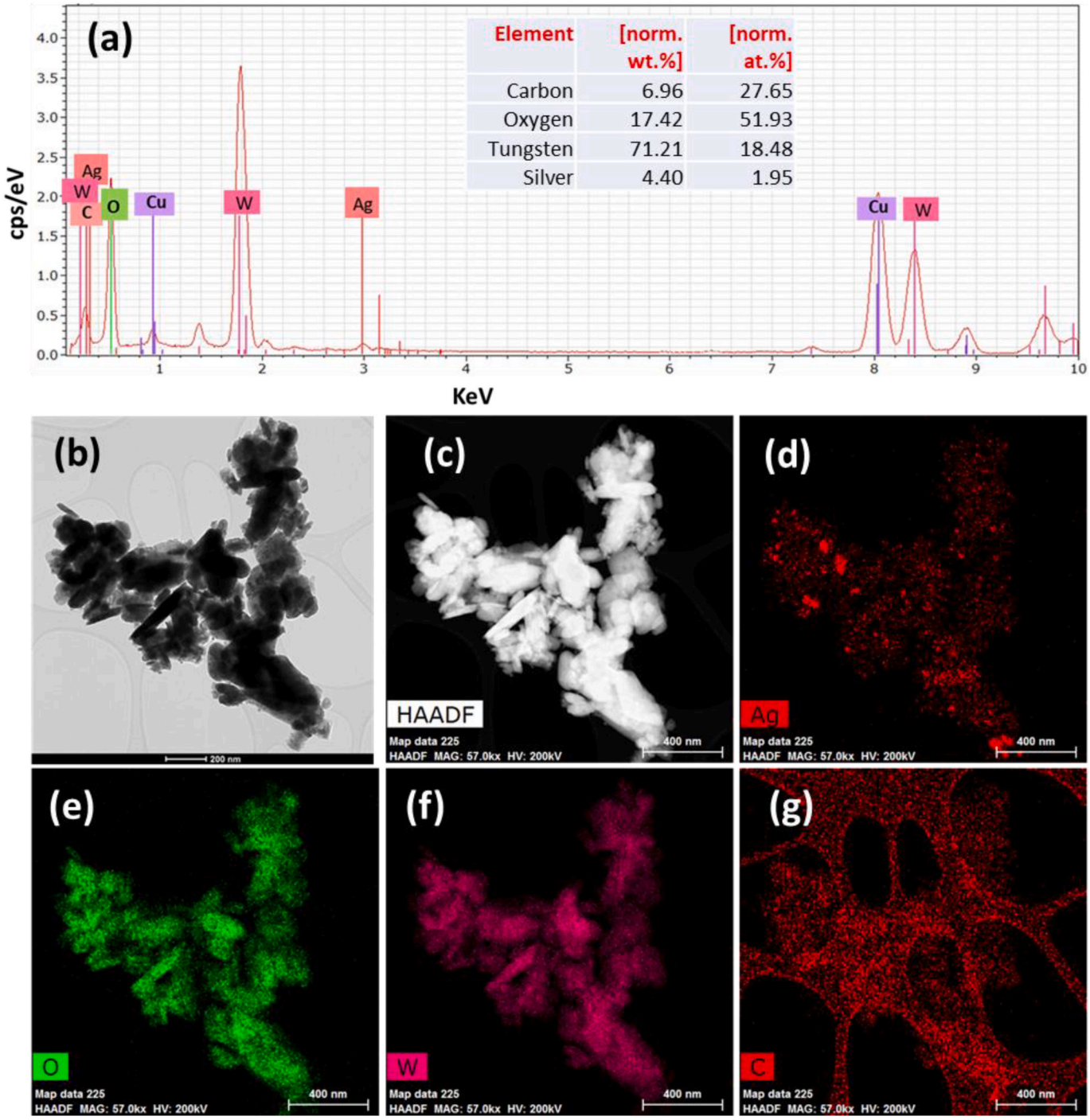

Fig. 2. TEM- EDS mapping of Ag/WO_3 containing 1% Ag. (a) High resolution (HRTEM) of Ag/WO_3; (b) Scanning TEM (STEM)–high-angle annular dark-field (HAADF); (c-g) Elemental mapping of Ag/WO_3.

WO_3 catalysts after 60 min reaction time are 71.7%, 71.6%, and 76.6%, respectively; they are all higher than WO_3 and MB without photocatalyst (0.00269 min^{-1}) having 67.4% and 19.3% degradation efficiencies, respectively. Compared to pristine TiO_2, it was reported that it presented a degradation percentage of about 23.5% [43]. The results of photocatalytic degradation of MB for bare and Ag (0.1%, 0.5%, and 1%) loaded WO_3 catalysts imply that the Ag loading has enhanced the photocatalytic degradation activity of WO_3. 1% Ag/WO_3 had superior photocatalytic activity than the other composites. The work of Khan et al. addressed Ag loading behavior, and it has been found that the photocatalytic activity of the catalyst increased upon increasing Ag loadings [36].

4.2. *Effect of pretreatment*

The pretreatment (calcination) effect is a necessary parameter to study, as it is mainly used to eliminate volatile compounds, water, or oxidize a substance, which is known as a purification process. This was proven by Imam and Chopra, where they found that the Ag/WO_3 band gap was significantly lowered upon pretreatment, implying better photocatalytic activity [44]. High-temperature heat treatment causes WO_3 to produce oxygen vacancy defects. These defects reduce the bandgap of

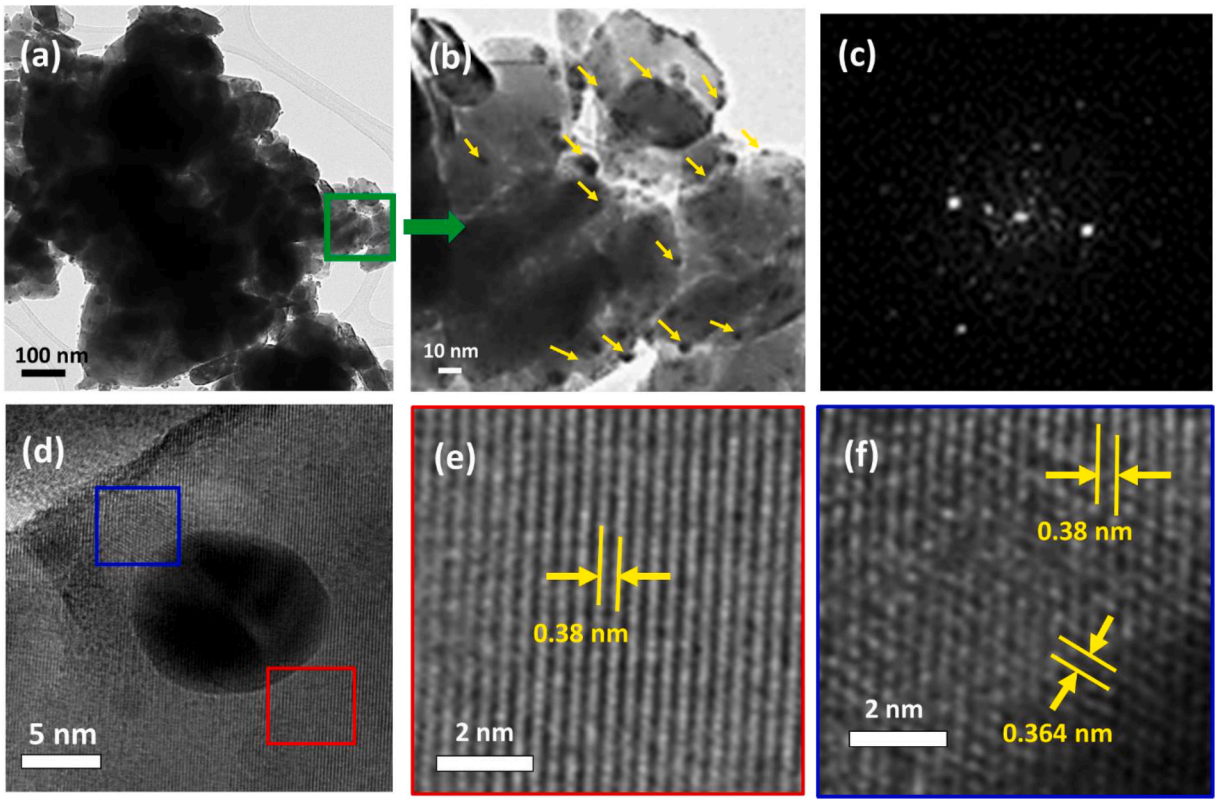

Fig. 3. High-resolution Transmission Electron Microscope (HRTEM) of Ag/WO_3 and the corresponding periodicity at a different level of magnifications.

1% Ag/WO_3 and improve photogenerated carriers' separation efficiency, resulting in high photocatalytic activity [45]. In this work, the effect of pretreatment was studied by performing photocatalytic degradation of aqueous MB solution on calcined/not calcined 1% Ag/WO_3 under visible light irradiation for 60 min reaction time in the presence of 0.1 M $NaBH_4$. The photocatalytic performance is carried out under similar conditions as in all experiments. Fig. 7 (a) indicates the relative (C_t/C_0) concentration of MB versus the reaction time, representing the response of photocatalytic activities of calcined/not calcined 1% Ag/WO_3. The plot illustrates that pretreated 1% Ag/WO_3 had higher photocatalytic activity towards MB degradation. The degradation data were fit using pseudo-first-order kinetics. Table 3 summarizes the reaction rate constant and degradation efficiencies for calcined/not-calcined 1% Ag/WO_3 and MB without catalyst. Fig. 7 (b) confirms the higher photocatalytic activity of calcined 1% Ag/WO_3 (0.01637 min-1), which is 1.5 times faster when compared to not-calcined 1% Ag/WO_3 (0.01127 min^{-1}). The degradation efficiencies achieved by pretreated/untreated 1% Ag/WO_3 are 76.6% and 66.6%, respectively. As predicted, the fabricated 1% Ag/WO_3 (pretreated) photocatalyst showed an improved photocatalytic performance, which indicates that the pretreatment had a considerable influence on the photocatalytic behavior of the photocatalysts. Therefore, pretreated 1% Ag/WO_3 is fixed as an optimized photocatalyst for the photodegradation of MB in irradiation conditions.

4.3. Comparison between photocatalysis performance under visible and UV light irradiation

The photocatalytic performance of the synthesized catalyst toward MB degradation under visible as compared to higher energy UV light, the photocatalytic performance of 1% Ag/WO_3 under both lights is summarized in table S1. Fig. S3 (a) indicates the relative (C_t/C_0) concentration of MB versus the reaction time of 1% Ag/WO_3. The plot illustrates that 1% Ag/WO_3 had higher photocatalytic activity towards MB degradation under UV irradiation. The degradation data were fit using pseudo-first-order kinetics. Fig. S3 (b) confirms the higher photocatalytic activity of 1% Ag/WO_3 under UV irradiation (0.02427 min^{-1}), which is 1 time faster when compared under visible irradiation (0.01682 min^{-1}). The degradation efficiencies of 1% Ag/WO_3 achieved under UV vs. visible irradiation are 90% and 80%, respectively. The higher photocatalytic activity of 1% Ag/WO_3 under UV can be attributed to UV irradiation's higher energy [46]. It was demonstrated by Çifçi et al. that MB removal efficiencies under UV and visible light irradiation of 99.2% and 44.5% for %1 Ag-doped the TiO_2, respectively [47].

4.4. Kinetics study of photocatalytic performance as a function of photocatalyst dose

The photocatalytic performance of pretreated 1% Ag/WO_3 was further investigated by studying the effect of catalyst dose (0.1–1 g/L) and observing the degradation of aqueous MB solution. Fig. 8 (a) demonstrates how the absorption spectra of MB changes when an aqueous suspension is irradiated in the presence of 1% Ag/WO_3 (1 g/L). It shows that as the irradiation period increases, MB dye's characteristic absorption peak at 664 nm decreases significantly. MB's maximum absorption wavelength at 664 nm changes to lower values (hypsochromic shift). The formation of reaction intermediates with absorption maxima at shorter wavelengths than MB is known to cause this change [48].

Fig. 8 (b) indicates the relative (C_t/C_0) concentration of MB versus the reaction time, which represents the response of different 1% Ag/WO_3 doses (0.1–1 g/L). It shows that the removal of MB dye increases as the photocatalyst increases. The degradation data of different catalyst doses were fit using pseudo-first-order kinetics. Table 4 summarizes the reaction rate constant and degradation efficiencies for 1% Ag/WO_3 in different doses and MB without catalyst. As illustrated in Fig. 8 (c), the photocatalytic degradation reaction rate constants for 0.1 g/L, 0.2 g/L, 0.5 g/L, and 1 g/L are 0.00426 cm^{-1}, 0.00587 cm^{-1}, 0.00928 cm^{-1}, 0.01682 cm^{-1}, respectively. The results show that 1 g/L photocatalyst

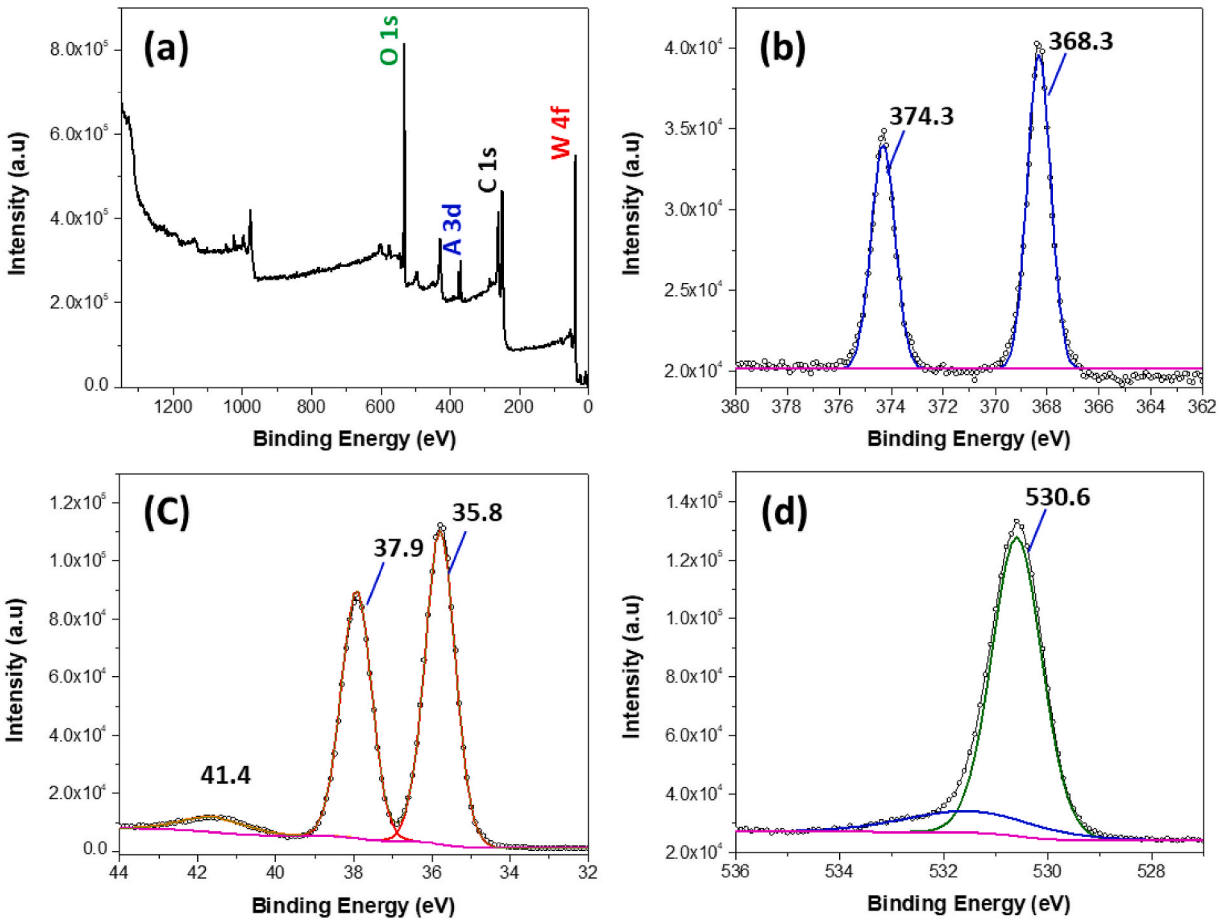

Fig. 4. Room-temperature X-ray photoelectron spectra (XPS) of Ag/WO_3 sample and peak fitting XPS survey scan of the sample after heat treatment at 300 (a). High-resolution scan of W, Ag, and O with the corresponding deconvoluted peaks (b–d).

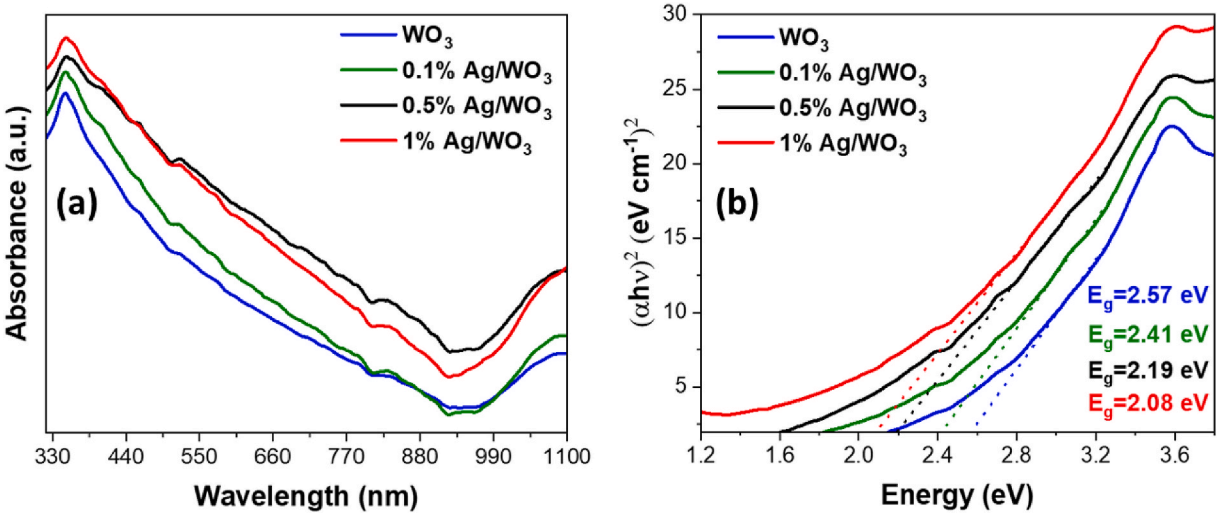

Fig. 5. UV–Visible absorption spectra (a) of bare WO_3 and Ag (0.1%, 0.5%, 1%) loaded WO_3 photocatalysts and their corresponding Tauc plot (b).

dose is 4 times faster than 0.1 g/L, 3 times faster than 0.2 g/L, and 2 times faster than 0.5 g/L in reaction rate constants. The degradation efficiencies achieved using different catalyst doses (0.1, 0.2, 0.5, and 1 g/L) are 33.6%, 42.1%, 58.3%, and 80%, respectively. It can be concluded that as the catalyst dose increases, the photocatalytic activity increases towards MB removal. Consequently, a fixed photocatalyst concentration of 1 g/L is further used.

MB photocatalytic degradation experiments demonstrated that 1% Ag/WO3 photocatalyst has outstanding MB removal activity under visible light irradiation. Fig. 8 (d) shows an apparent MB degradation rate constant (k_{app}) as a function of 1% Ag/WO_3 photocatalyst dose under visible light irradiation. Our results showed that the MB degradation rate constant for 1% Ag/WO_3 photocatalyst under visible light is 0.01379 min–1, which is 1 time faster than WO_3 photocatalyst (0.01278

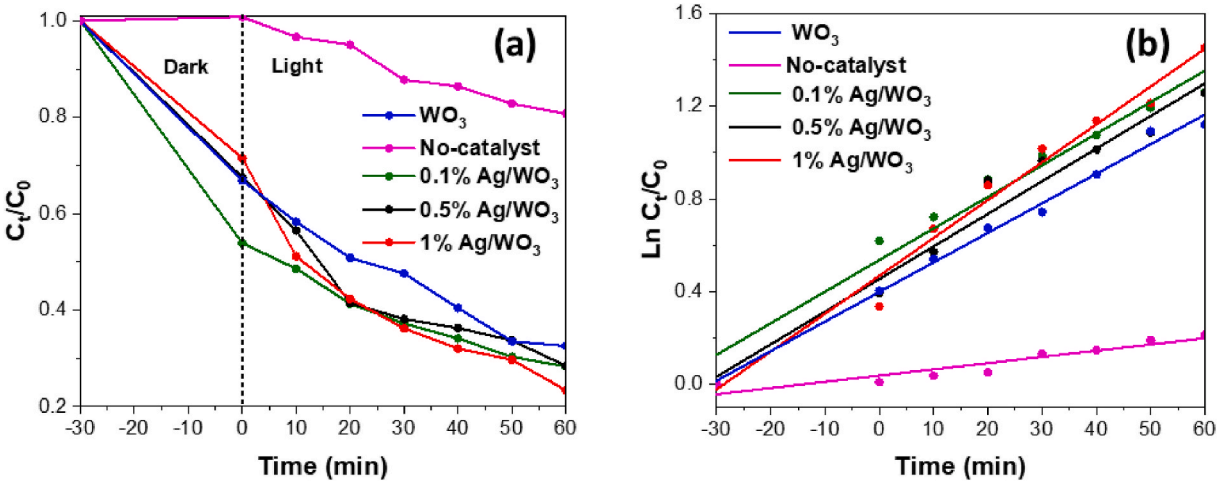

Fig. 6. (a) Photocatalytic degradation of aqueous MB solution employing the effect of different Ag loadings (0.1%, 0.5%, 1%) at WO_3 in the presence of 0.1 M $NaBH_4$ under visible-light irradiation; (b) Pseudo-first order kinetics of the degradation over Ag (0.1%, 0.5%, 1%)/WO_3. Reaction conditions: visible light irradiation: 400 W, 5 mg/L MB, room temperature (23–25 °C).

Table 2
Reaction rate constants and degradation efficiencies for bare WO_3, Ag (0.1%, 0.5%, 1%) loaded WO_3 photocatalysts and MB without catalyst.

Material	Reaction rate constant (min^{-1})	Degradation efficiency (%)
WO_3	0.01278	67.4
No-catalyst	0.00269	19.3
0.1% Ag@WO_3	0.01366	71.7
0.5% Ag@WO_3	0.0141	71.6
1% Ag@WO_3	0.01682	76.6

min^{-1}).

5. Stability and recyclability test

From the standpoint of practical application, the stability of the catalyst has always been a critical component. To assess the photostability, the photocatalytic activity of 1% Ag/WO_3 (1 g/L), which presented the most outstanding results, was tested for the photocatalytic degradation of the aqueous MB solution. The recyclability test was carried out up to four times. After photocatalytic reactions, catalyst powders were collected by filtration using a 0.45 μm PTFE syringe filter, washed with UPW, and dried for the next photoreaction cycle, with the results depicted in Fig. 9. After four cycles, the catalyst showed a slight reduction in photocatalytic activity, implying the catalyst's excellent stability under visible light irradiation.

The chemical structure of bare WO_3, 1% Ag/WO_3, and 1% Ag/WO_3 before and after MB degradation was characterized using FTIR spectroscopy, as shown in Fig. S4. The FTIR shows no significant change in the structure after MB photocatalytic degradation, implying the photocatalyst's stability.

The repeatability test was performed by repeating the same procedure of the photocatalytic activity test four times on 1% Ag/WO_3, and values are roughly the same in every run. Fig. S5 shows an excellent

Table 3
Reaction rate constants and degradation efficiencies for calcined/not-calcined 1% Ag/WO_3 and MB without catalyst.

Material	Reaction rate constant (min^{-1})	Degradation efficiency (%)
No-catalyst	0.00269	19.3
No calcination	0.1127	66.6
Calcination	0.01682	76.6

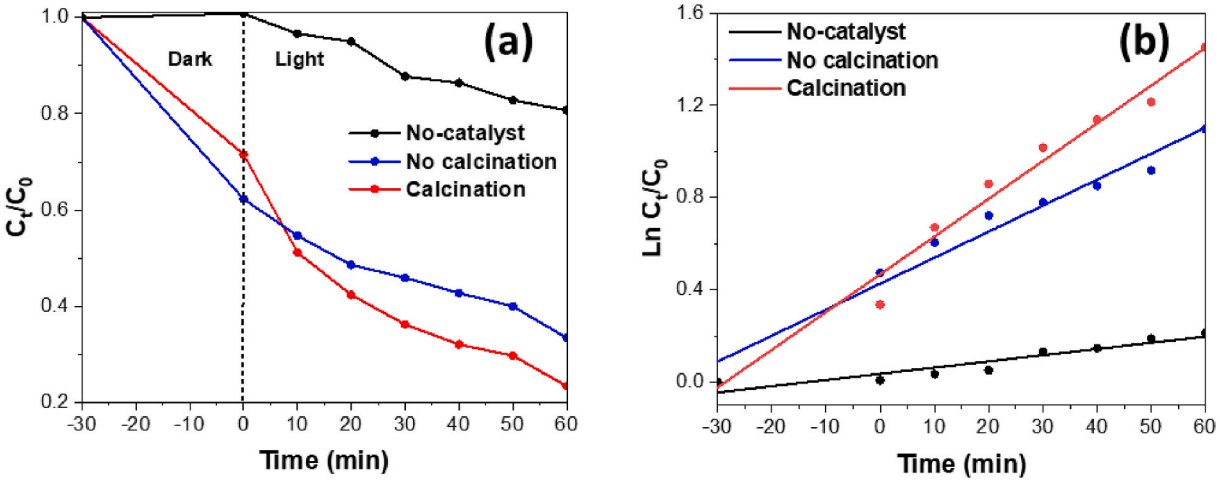

Fig. 7. (A) Photocatalytic degradation of aqueous MB solution in the presence of 1% Ag/WO_3 and 0.1 M $NaBH_4$ employing the effect of pretreatment under visible-light irradiation; (B) Pseudo-first order kinetics of the degradation over 1% Ag/WO_3. Reaction conditions: visible light irradiation: 400 W, 5 mg/L MB, room temperature (23–25 °C).

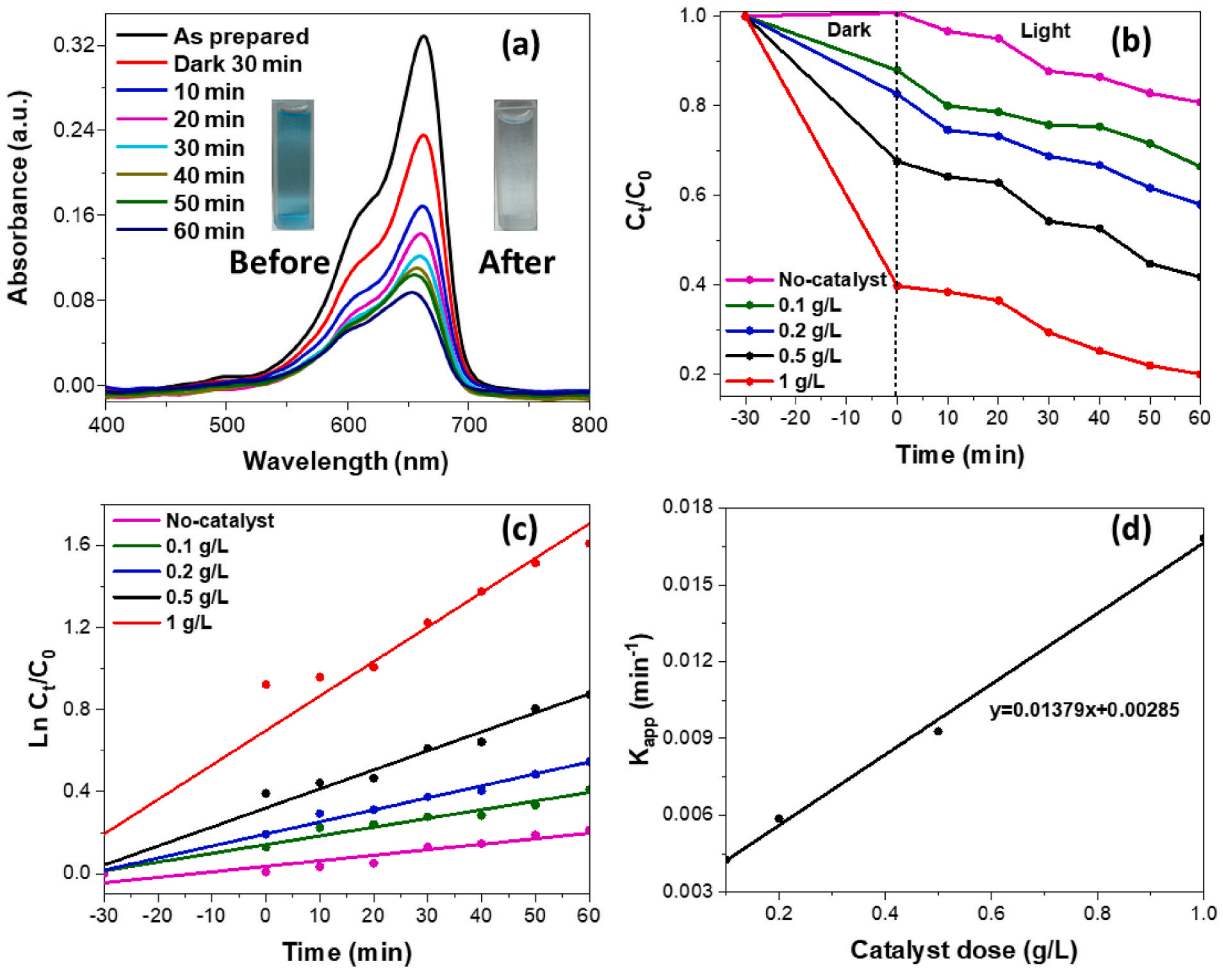

Fig. 8. (a) UV–Visible absorption spectra of aqueous MB solution with reaction time in the presence of 1% Ag/WO_3 (1 g/L) and 0.1 M NaBH4 under visible-light irradiation, and MB color change before and after degradation (inset); (b) Photocatalytic degradation of aqueous MB solution in the presence of 1% Ag/WO_3 employing different catalyst doses (0.1–1 g/L) in the presence of 0.1 M NaBH4 under visible-light irradiation; (c) Pseudo-first order kinetics for the degradation over 1% Ag/WO_3 (0.1–1 g/L); (d) Apparent MB degradation rate constant (k_{app}) as a function of 1% Ag/WO_3 photocatalyst concentration under visible light irradiation. Reaction conditions: visible light irradiation: 400 W, 5 mg/L MB, room temperature (23–25 °C).

Table 4
Reaction rate constants and degradation efficiencies for 1% Ag/WO_3 in different doses and MB without catalyst.

Material	Reaction rate constant (min^{-1})	Degradation efficiency (%)
No-catalyst	0.00269	19.3
0.1 g/L	0.00426	33.6
0.2 g/L	0.00587	42.1
0.5 g/L	0.00928	58.3
1 g/L	0.01682	76.6

repeatability performance towards MB degradation using 1% Ag/WO_3 (1 g/L) under visible light irradiation [29].

6. MB degradation mechanism on Ag/WO_3 under visible light irradiation

To fully comprehend the enhanced photocatalytic activity, further research into the photocatalytic mechanism is needed. Here, it is discussed in detail in terms of the work functions. According to the literature, the work functions of WO_3 and Ag are 5.7 eV and 4.26 eV, respectively. As Ag comes into contact with WO_3, electrons can transfer from Ag to WO_3's CB, achieving Fermi level equilibration. As a result, excess electrons accumulate on the surface of WO_3, while excess positive charge accumulates on the surface of Ag, forming a deflexed energy

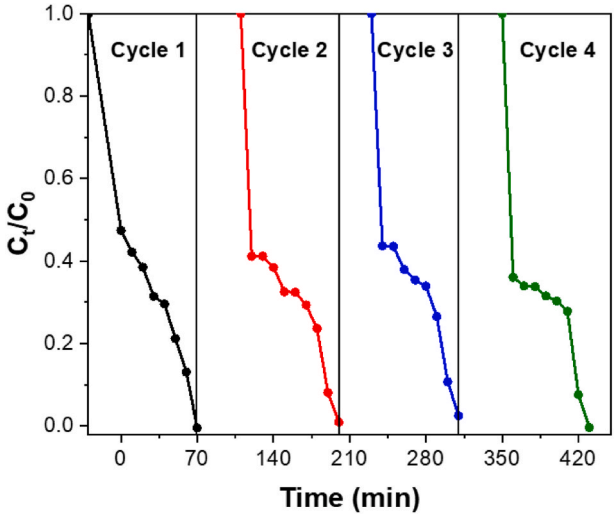

Fig. 9. Stability and recyclability test of 1% Ag/WO_3 for photocatalytic degradation of aqueous MB solution in the presence of 0.1 M NaBH4 under visible light irradiation. Reaction conditions: visible light irradiation: 400 W, 5 mg/L MB, room temperature (23–25 °C).

band at the Ag/WO_3 interface. Furthermore, the deflexed energy band in the space charge region enables the rapid transfer of the as-excited electrons from WO_3 to Ag nanoparticles, which reduces the recombination of the photogenerated electron-hole pairs. Since WO_3 has a low CB level that is more positive than the given potential for the single-electron reduction of O_2, the multi-electron reduction of O_2 will move electrons accumulated at Ag nanoparticles to surface-adsorbed oxygen molecules to form H_2O_2 [49].

The following steps summarize the proposed mechanism for MB degradation (Fig. 10). First, visible light irradiation allows electrons in the VB to transfer into the CB. Consequently, holes (h^+) and electrons (e^-) are formed at the surface of the WO_3 photocatalyst. Oxygen vacancy defects then trap the photogenerated electrons on the surface. Then, the holes react with hydroxide ions, while electrons react with dissolved oxygen to produce $OH^\bullet$, which breaks down MB dye into harmless gases like carbon dioxide and water. Moreover, hydrogen peroxide reacts with electrons to produce more $OH^\bullet$ to speed up the dye's decomposition.

$$Ag/WO_3 + \text{visible light} \rightarrow h^+ \text{(hole)} + e^- \text{(electron)} \quad (4)$$

$$h^+ + H_2O \rightarrow H^+ + OH^- \quad (5)$$

$$h^+ + OH- \rightarrow OH^\bullet \quad (6)$$

$$e^- + O_2 \rightarrow O_2{}^{\bullet-} \quad (7)$$

$$O_2{}^{\bullet-} + e- + 2H^+ \rightarrow H_2O_2 \quad (8)$$

$$O_2{}^{\bullet-} + H_2O_2 \rightarrow OH^\bullet + OH^- + O_2 \quad (9)$$

$$OH^\bullet + \text{dye} \rightarrow \text{nontoxic products} + CO_2\uparrow \quad (10)$$

$$O_2{}^{\bullet-} + \text{dye} \rightarrow \text{nontoxic products} + CO_2\uparrow \quad (11)$$

7. Antibacterial activity results

Antibacterial activity of 1% Ag/WO_3 was tested against two bacterial strains of Gram-negative *E. Coli* and the Gram-positive *S. aureus*. The suspension test method was utilized to test for antibacterial activity of 1% Ag/WO_3 in light and dark conditions at different concentrations (0–1 g/L). Fig. 11 illustrates the results of the antibacterial activity of 1% Ag/WO_3 toward *E. coli*. And *S. aureus* growth inhibition under ambient light and in dark conditions.

Fig. 11 shows dose-dependent inhibition in bacterial growth upon exposure to different concentrations of 1% Ag/WO_3 for both *S. aureus* and *E. Coli* under light and dark conditions. As the concentration increased, the bacterial growth decreased compared to the normal growth curve in *E. coli* and *S. aureus* (Fig. 11). This suggests a specific effect of the 1% Ag/WO_3 nanoparticle. It has been noticed that 1% $AgWO_3$ nanoparticles exhibited a better bactericidal effect on Gram-negative bacteria (*E. coli*) than the Gram-positive (*S. aureus*). This difference might be due to the differences in the cell wall structure.

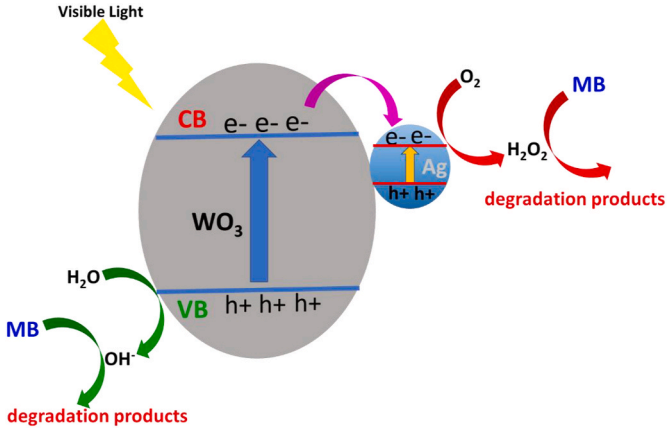

Fig. 10. MB photodegradation reaction mechanism on Ag/WO_3 under visible light irradiation.

Gram-positive bacteria have a thick cell wall composed of many layers of peptidoglycan and teichoic acids, whereas Gram-negative bacteria cell walls are relatively thin with an outer membrane with lipopolysaccharides and lipoprotein bilayers [50]. Therefore, the thick Gram-positive bacteria cellular wall might limit the uptake of the nanoparticle drug or resist drug exposure, in contrast to the Gram-negative bacteria [51]. The mechanism of action of antibacterial 1% Ag/WO_3 nanoparticles is not well understood. However, the electrostatic attraction between bacterial cells and nanoparticles was determined to play a crucial role. The attraction between the positively charged Ag nanoparticles and the negatively charged bacterial cell membrane confer the electrostatic attraction, facilitating Ag nanoparticles' attachment and entry into the cell membrane [52]. A previous study using *E. coli* demonstrated that Ag nanoparticles penetrate through the membrane and disrupt protein synthesis, leading to structural changes and death [53]. In addition, another study investigated the effect of silver nanoparticles on the growth, permeability, and morphology of *E. coli.* The results suggest that silver nanoparticles damaged the bacterial cell membrane structure and reduced the activity of membranous enzymes, eventually leading to bacterial death [54]. Therefore, further analysis and testing using scanning electron microscopy (SEM) and transmission electron microscopy (TEM) needs to be performed to fully understand the mechanism of action of 1% Ag/WO_3 in dark and light conditions.

Metallic Ag NPs and the Ag + it releases are both effective antibacterial agents. Although the specific antibacterial mechanism is unclear, several potential theories include the production of reactive oxygen species (ROS) and the breakdown of cell walls and/or membranes. Two factors contribute to the antibacterial performance of 1% Ag/WO3 composite. First, the interaction of 1% Ag/WO3 composite with the surface of bacteria disrupted the bacterial cell wall, allowing Ag NPs and Ag + ions to enter. Once inside the bacteria, Ag NPs and/or Ag^+ ions interact with many targets simultaneously, including enzymes, DNA, and proteins, through various metabolic pathways, disrupting cell metabolic function and triggering bacteria death. Second, 1% Ag/WO_3 composite could result in the generation of ROS. Oxidative stress is caused by species such as $O_2{}^-$, H_2O_2, and $OH^\bullet$ in excessive concentrations; bacteria can then suffer substantial damage, leading to cell death [55].

8. Conclusion

Nanocrystalline silver (Ag), supported on tungsten oxide (WO_3) nanoparticles, were successfully synthesized via the deposition-precipitation synthesis technique, which was composed of mainly monoclinic sheet-like morphology tungsten oxide (>500 nm) with a few spherical particles (<200 nm), and small (<3 nm) and well-dispersed metallic silver nanoparticles on the surface as confirmed by XRD, TEM-EDS, and XPS. Furthermore, the deposition of Ag onto the WO_3 surface reduces the bandgap energy (from 2.6 to 2.1 eV at 1% Ag loading), evidenced by a redshift and visible radiation emission as confirmed by UV–Vis spectroscopy. The prepared heterogeneous 1% Ag/WO_3 photocatalyst demonstrated significant MB degradation under visible light compatible with the degradation level under UV light radiation. Dose-dependent MB photodegradation kinetics followed the pseudo-first-order kinetics suggesting that the photocatalytic activity scales up with catalyst dose. Moreover, the photocatalyst demonstrated effective dose-dependent inhibition against Gram-negative *E. Coli* and the Gram-positive *S. aureus* under ambient light and dark conditions, with a stronger effect under light. The effective dispersion of Ag within the WO3 support enhanced the electron-hole pair separation rate by entrapping and transferring the photo-excited electrons, which

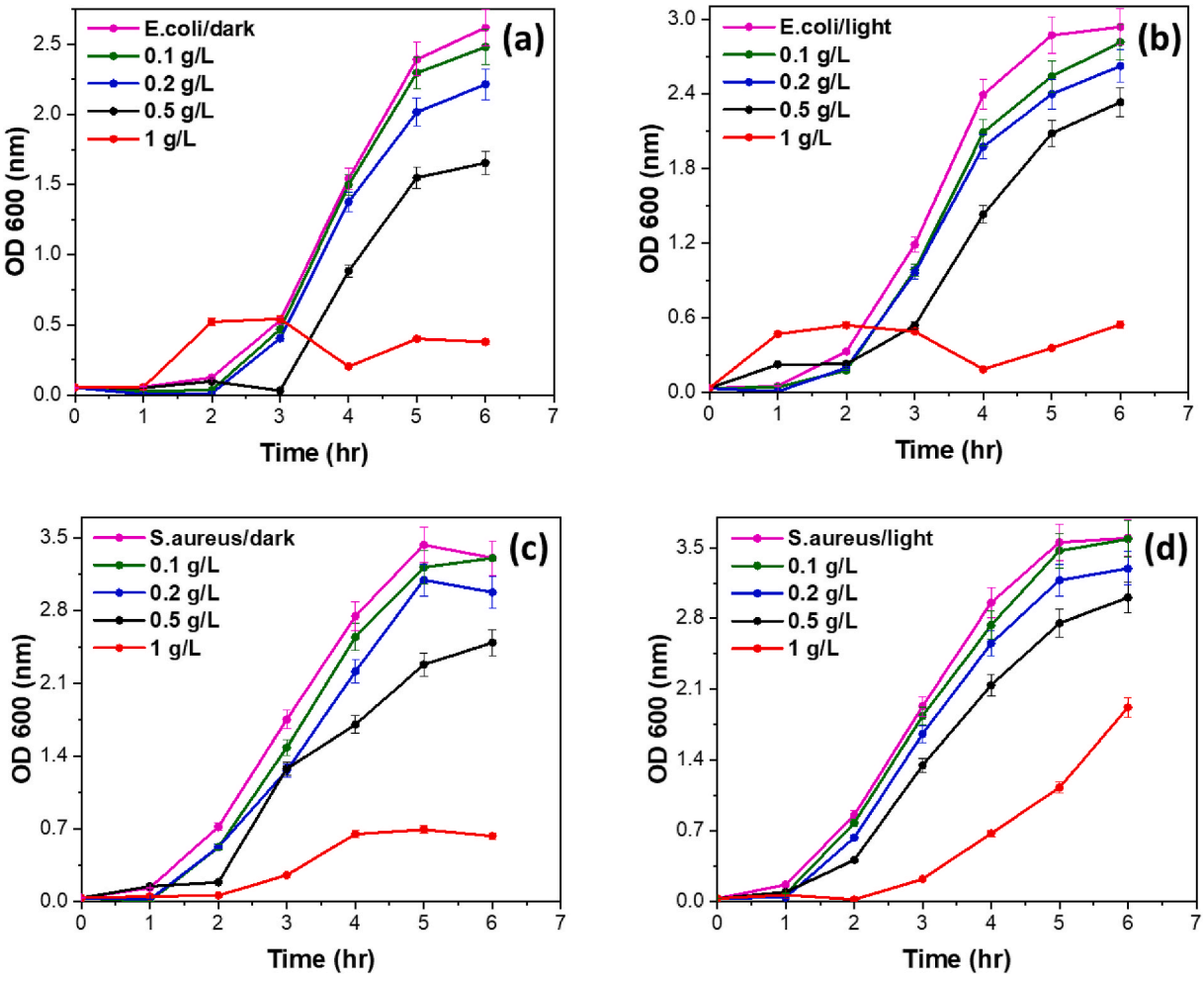

Fig. 11. Dose-dependent inhibition of *E. coli* and *S. aureus* upon incubation with 1% Ag/WO_3. Bacterial growth of (a) *E. coli* in the dark; (b) *E. coli* in light, (c) *S. aureus* in the dark; and (d) *S. aureus* in light, in the presence of different 1%Ag/WO_3 concentrations (0.1–1 g/L). Compared to the control, the 1%Ag/WO3 significantly inhibited *E. coli* and *S. aureus* growth after 6 h as the concentration increased. $p \leq 0.05$, $p \leq 0.01$, $p \leq 0.001$.

increased the reactive species that aid the degradation efficiency and inhibition of bacterial growth. Overall, the Ag/WO_3 photocatalyst demonstrates excellent stability and recyclability, photocatalytic activity, and antibacterial properties, making it applicable in many applications such as water purification and surface sterilization under visible light and dark conditions.

Declaration of competing interest

The authors declare that they have no known competing financial interests or personal relationships that could have appeared to influence the work reported in this paper.

Acknowledgments

This work was supported by Qatar Foundation Research Development and Innovation (QFRDI) grant number: [TDF02-0616-190004] and VCUart Qatar/Qatar Foundation-Nanotechnology and Textile Research Lab fund grant number [HQ1240].

Appendix A. Supplementary data

Supplementary data to this article can be found online at https://doi.org/10.1016/j.rineng.2021.100313.

References

[1] A.R. Baqer, A.A. Beddai, M.M. Farhan, B.A. Badday, M.K. Mejbel, Efficient coating of titanium composite electrodes with various metal oxides for electrochemical removal of ammonia, Res. Eng. 9 (2021) 100199.
[2] A.K.M. Nayab-Ul-Hossain, S.K. Sela, S.B. Sadeque, Recycling of dyed fiber waste to minimize resistance and to prepare electro thermal conductive bar, Res. Eng. 3 (2019) 100022.
[3] S. Ahmed, M.G. Rasul, W.N. Martens, R. Brown, M.A. Hashib, Advances in heterogeneous photocatalytic degradation of phenols and dyes in wastewater: a review, Water Air Soil Pollut. 215 (2010) 3–29.
[4] A.R. Khataee, M.B. Kasiri, Photocatalytic degradation of organic dyes in the presence of nanostructured titanium dioxide: influence of the chemical structure of dyes, J. Mol. Catal. Chem. 328 (2010) 8–26.
[5] A. Raghunath, E. Perumal, Metal oxide nanoparticles as antimicrobial agents: a promise for the future, Int. J. Antimicrob. Agents 49 (2017) 137–152.
[6] E. Sánchez-López, D. Gomes, G. Esteruelas, L. Bonilla, A.L. Lopez-Machado, R. Galindo, A. Cano, M. Espina, M. Ettcheto, A. Camins, A.M. Silva, A. Durazzo, A. Santini, M.L. Garcia, E.B. Souto, Metal-based nanoparticles as antimicrobial agents: an overview, Nanomaterials 10 (2020) 292.
[7] V.K. Yemmireddy, Y.-C. Hung, Using photocatalyst metal oxides as antimicrobial surface coatings to ensure food safety—opportunities and challenges, Compr. Rev. Food Sci. Food Saf. 16 (2017) 617–631.
[8] T. Bak, J. Nowotny, M. Rekas, C.C. Sorrell, Photo-electrochemical hydrogen generation from water using solar energy. Materials-related aspects, Int. J. Hydrogen Energy 27 (2002) 991–1022.
[9] R. Bhargava, S. Khan, Fabrication of WO3–reduced graphene oxide (WO3–G) nanocomposite for enhanced optical and electrical properties, J. Mater. Sci. Mater. Electron. 31 (2020) 8370–8384.
[10] R. Nagarjuna, S. Challagulla, P. Sahu, S. Roy, R. Ganesan, Polymerizable sol–gel synthesis of nano-crystalline WO 3 and its photocatalytic Cr(VI) reduction under visible light, Adv. Powder Technol. 28 (2017) 3265–3273.

[11] S. Malato, P. Fernández-Ibáñez, M.I. Maldonado, J. Blanco, W. Gernjak, Decontamination and disinfection of water by solar photocatalysis: recent overview and trends, Catal. Today 147 (2009) 1–59.
[12] M.A. Rauf, S.S. Ashraf, Fundamental principles and application of heterogeneous photocatalytic degradation of dyes in solution, Chem. Eng. J. 151 (2009) 10–18.
[13] S.-H. Lee, H.M. Cheong, P. Liu, D. Smith, C.E. Tracy, A. Mascanrenhas, J.R. Pitts, S. K. Deb, Gasochromic mechanism in a-WO3 thin films based on Raman spectroscopic studies, J. Appl. Phys. 88 (2000) 3076–3078.
[14] C. Avellaneda, Intercalation in WO3 and WO3:Li films, Solid State Ionics 165 (2003) 59–64.
[15] E. György, G. Socol, I.N. Mihailescu, C. Ducu, S. Ciuca, Structural and optical characterization of WO3 thin films for gas sensor applications, J. Appl. Phys. 97 (2005), 093527.
[16] R.K. Matharu, L. Ciric, G. Ren, M. Edirisinghe, Comparative study of the antimicrobial effects of tungsten nanoparticles and tungsten nanocomposite fibres on hospital acquired bacterial and viral pathogens, Nanomaterials 10 (2020) 1017.
[17] J. Chen, J. Cen, X. Xu, X. Li, The application of heterogeneous visible light photocatalysts in organic synthesis, Catal. Sci. Technol. 6 (2016) 349–362.
[18] S. Baruah, R.F. Rafique, J. Dutta, Visible light photocatalysis BY tailoring crystal defects IN zinc oxide nanostructures, Nano (2008) 399–407, 03.
[19] W. Mu, X. Xie, X. Li, R. Zhang, Q. Yu, K. Lv, H. Wei, Y. Jian, Characterizations of Nb-doped WO3 nanomaterials and their enhanced photocatalytic performance, RSC Adv. 4 (2014) 36064–36070.
[20] R. Malik, P.S. Rana, V.K. Tomer, V. Chaudhary, S.P. Nehra, S.J.M. Duhan, M. Materials, Nano gold supported on ordered mesoporous WO3/SBA-15 hybrid nanocomposite for oxidative decolorization of azo dye 225 (2016) 245–254.
[21] K. Saoud, R. Alsoubaihi, N. Bensalah, T. Bora, M. Bertino, J. Dutta, Synthesis of supported silver nano-spheres on zinc oxide nanorods for visible light photocatalytic applications, Mater. Res. Bull. 63 (2015) 134–140.
[22] K. Saoud, R. Al- Soubaih, S. Saeed, N. Bensalah, M. Al-Fandi, T. Singh, Heterogeneous Ag and ZnO based photocatalytic for waste water treatment under different irradiation conditions, J. Mater. Environ. Sci. 9 (2018) 400–413.
[23] T.H. Jeon, D. Monllor–Satoca, G.h. Moon, W. Kim, H.i. Kim, D.W. Bahnemann, H. Park, W. Choi, Ag(I) ions working as a hole-transfer mediator in photoelectrocatalytic water oxidation on WO3 film, Nat. Commun. 11 (2020) 967.
[24] A.Y. Vasil'kov, R.I. Dovnar, S.M. Smotryn, N.N. Iaskevich, A.V. Naumkin, Plasmon resonance of silver nanoparticles as a method of increasing their antibacterial action, Antibiotics (2018) 7.
[25] H. Ren, X. Gou, Q. Yang, Ultrathin Ag nanoparticles anchored on urchin-like WO3·0.33H2O for enhanced photocatalytic performance, RSC Adv. 7 (2017) 12085–12088.
[26] A.A. Fairuzi, N.N. Bonnia, R.M. Akhir, M.A. Abrani, H.M. Akil, Degradation of methylene blue using silver nanoparticles synthesized from imperata cylindrica aqueous extract, IOP Conf. Ser. Earth Environ. Sci. 105 (2018), 012018.
[27] C. Lin, K. Tao, D. Hua, Z. Ma, S. Zhou, Size effect of gold nanoparticles in catalytic reduction of p-nitrophenol with NaBH4, Molecules 18 (2013) 12609–12620.
[28] A. Nafady Sirajuddin, H.I. Afridi, S. Sara, A. Shah, A. Niaz, Direct synthesis and stabilization of Bi-sized cysteine-derived gold nanoparticles: reduction catalyst for methylene blue, J. Iran. Chem. Soc. 8 (2011) S34–S43.
[29] S. Sun, W. Wang, S. Zeng, M. Shang, L. Zhang, Preparation of ordered mesoporous Ag/WO3 and its highly efficient degradation of acetaldehyde under visible-light irradiation, J. Hazard Mater. 178 (2010) 427–433.
[30] L. Xu, M.-L. Yin, S.F. Liu, Ag(x)@WO₃ core-shell nanostructure for LSP enhanced chemical sensors, Sci. Rep. 4 (2014), 6745-6745.
[31] T. Tomoharu, K. Tadashi, T. Kenta, N. Naohiro, H. Yasuhiko, K. Sasaki, K. Kotaro, Growth and Structure Analysis of Tungsten Oxide Nanorods Using Environmental TEM, 2010 8th International Vacuum Electron Sources Conference and Nanocarbon, IEEE, 2010.
[32] S. Mohammed Harshulkhan, K. Janaki, G. Velraj, R. Sakthi Ganapathy, S. Krishnaraj, Structural and optical properties of Ag doped tungsten oxide (WO3) by microwave-assisted chemical route, J. Mater. Sci. Mater. Electron. 27 (2015) 3158–3163.
[33] R. Ambroziak, M. Hołdyński, T. Płociński, M. Pisarek, A. Kudelski, Cubic silver nanoparticles fixed on TiO2 nanotubes as simple and efficient substrates for surface enhanced Raman scattering, Materials 12 (2019) 3373.
[34] L.F. Lopes, F.M. Pontes, L.O. Garcia, D.S.L. Pontes, D. Padovani, A.J. Chiquito, S. R. Teixeira, Y.N. Colmenares, V.R. Mastelaro, E. Longo, Silver-controlled evolution of morphological, structural, and optical properties of three-dimensional hierarchical WO 3 structures synthesized from hydrothermal method, J. Alloys Compd. 736 (2018) 143–151.
[35] D. Gogova, K. Gesheva, A. Szekeres, M. Sendova-Vassileva, Structural and optical properties of CVD thin tungsten oxide films, Phys. Status Solidi 176 (1999) 969–984.
[36] M. Khan, S. Kumar, T. Ahamad, A. Alhazaa, Enhancement of photocatalytic and electrochemical properties of hydrothermally synthesized WO 3 nanoparticles via Ag loading, J. Alloys Compd. (2018) 743.
[37] H. Najafi-Ashtiani, A. Bahari, S. Gholipour, S. Hoseinzadeh, Structural, optical and electrical properties of WO3–Ag nanocomposites for the electro-optical devices, Appl. Phys. A 124 (2017) 24.
[38] P. Hua-Feng, X. Xiang, Z. Li, Y.Q. Fu, X.-T. Zu, Hydrothermal synthesis and optical properties of hexagonal tungsten oxide nanocrystals assisted by ammonium tartrate, Phys. Status Solidi 209 (2012) 537–544.
[39] M. Desseigne, N. Dirany, V. Chevallier, M. Arab, Shape dependence of photosensitive properties of WO3 oxide for photocatalysis under solar light irradiation, Appl. Surf. Sci. 483 (2019) 313–323.
[40] J. Ding, Y. Chai, Q. Liu, X. Liu, J. Ren, W.-L. Dai, Selective deposition of silver nanoparticles onto WO3 nanorods with different facets: the correlation of facet-induced electron transport preference and photocatalytic activity, J. Phys. Chem. C 120 (2016) 4345–4353.
[41] S. Mohammed Harshulkhan, K. Janaki, G. Velraj, R. Sakthi Ganapthy, M. Nagarajan, Effect of Ag doping on structural, optical and photocatalytic activity of tungsten oxide (WO3) nanoparticles, J. Mater. Sci. Mater. Electron. 27 (2016) 4744–4751.
[42] M. Hu, X. Yan, X. Hu, R. Feng, M. Zhou, Synthesis of silver decorated silica nanoparticles with rough surfaces as adsorbent and catalyst for methylene blue removal, J. Sol. Gel Sci. Technol. 89 (2019) 754–763.
[43] R. Ren, Z. Wen, S. Cui, Y. Hou, X. Guo, J. Chen, Controllable synthesis and tunable photocatalytic properties of Ti3+-doped TiO2, Sci. Rep. 5 (2015) 10714.
[44] M.A. Imam, N. Chopra, Morphological, Structural and Optical Characterization of Bottom-Up Growth of Ag-WO3 Core-Shell Nano-Cube Heterostructures, 2017.
[45] Q. Liu, F. Wang, H. Lin, Y. Xie, N. Tong, J. Lin, X. Zhang, Z. Zhang, X. Wang, Surface oxygen vacancy and defect engineering of WO3 for improved visible light photocatalytic performance, Catal. Sci. Technol. (2018) 8.
[46] S. Singh, G. Madras, Photocatalytic degradation with combustion synthesized WO3 and WO3TiO2 mixed oxides under UV and visible light, Separ. Purif. Technol. 105 (2013) 79–89.
[47] D. Çifçi, Decolorization of methylene blue and methyl orange with Ag doped TiO2 under UV-A and UV-Visible conditions: process optimization by response surface method and toxicity evaluation, Global Nest J. 18 (2016) 371–380.
[48] G. Marbán, T.T. Vu, T. Valdés-Solís, A simple visible spectrum deconvolution technique to prevent the artefact induced by the hypsochromic shift from masking the concentration of methylene blue in photodegradation experiments, Appl. Catal. Gen. 402 (2011) 218–223.
[49] P. Dong, B. Yang, C. Liu, F. Xu, X. Xi, G. Hou, R. Shao, Highly enhanced photocatalytic activity of WO3 thin films loaded with Pt–Ag bimetallic alloy nanoparticles, RSC Adv. 7 (2017) 947–956.
[50] S. Brown, J.P. Santa Maria Jr., S. Walker, Wall teichoic acids of gram-positive bacteria 67 (2013) 313–336.
[51] E. Pazos-Ortiz, J.H. Roque-Ruiz, E.A. Hinojos-Márquez, J. López-Esparza, A. Donohué-Cornejo, J.C. Cuevas-González, L.F. Espinosa-Cristóbal, S.Y. Reyes-López, Dose-dependent Antimicrobial Activity of Silver Nanoparticles on Polycaprolactone Fibers against Gram-Positive and Gram-Negative Bacteria, 2017, p. 2017.
[52] T.C. Dakal, A. Kumar, R.S. Majumdar, V.J.F.i.m. Yadav, Mechanistic basis of antimicrobial actions of silver nanoparticles 7 (2016) 1831.
[53] C.S. Ciobanu, S.L. Iconaru, M.C. Chifiriuc, A. Costescu, P. Le Coustumer, D.J.B.R. I. Predoi, Synthesis and Antimicrobial Activity of Silver-Doped Hydroxyapatite Nanoparticles, 2013, p. 2013.
[54] W.-R. Li, X.-B. Xie, Q.-S. Shi, H.-Y. Zeng, O.-Y. You-Sheng, Y.-B.J.A.m. Chen, biotechnology, Antibacterial activity and mechanism of silver nanoparticles on Escherichia coli 85 (2010) 1115–1122.
[55] R. Capeli, T. Dapieve, J. Caierão, C. Dalmaschio, S. Teixeira, V. Mastelaro, Chiquito, M. Daldin Teodoro, E. Longo Domenegueti, L. Trindade, Pontes, T. Belmonte, Effect of hydrothermal temperature on the antibacterial and photocatalytic activity of WO 3 decorated with silver nanoparticles, J. Sol. Gel Sci. Technol. 97 (2021).